Thick lanthanum zirconate buffer layers from water-based precursor solutions on Ni-5%W substrates

Vyshnavi Narayanan [a], Petra Lommens [a], Klaartje De Buysser [a], Ruben Hühne [b], Isabel Van Driessche [a,*]

[a] SCRIPTS, Department of Inorganic and Physical Chemistry, Ghent University, Krijgslaan 281-S3, B-9000 Gent, Belgium
[b] IFW Dresden, Institute for Metallic Materials, Helmholtzstrasse 20, 01069 Dresden, Germany

ABSTRACT

In this work, water-based precursor solutions suitable for dip-coating of thick $La_2Zr_2O_7$ (LZO) buffer layers for coated conductors on Ni-5%W substrates were developed. The solutions were prepared based on chelate chemistry using water as the main solvent. The effect of polymer addition on the maximum crack-free thickness of the deposited films was investigated. This novel solution preparation method revealed the possibility to grow single, crack-free layers with thicknesses ranging 100–280 nm with good crystallinity and an in-plane grain misalignment with average FWHM of 6.55°. TEM studies illustrated the presence of nanovoids, typical for CSD–LZO films annealed under Ar-5%H$_2$ gas flow. The appropriate buffer layer action of the film in preventing the Ni diffusion was studied using XPS. It was found that the Ni diffusion was restricted to the first 30 nm of a 140 nm thick film. The surface texture of the film was improved using a seed layer.

© 2011 Elsevier Inc. All rights reserved.

1. Introduction

Lanthanum zirconate ($La_2Zr_2O_7$, LZO), being a pyrochlore material, is widely used for high temperature applications [1,2], thermal barrier coatings [3,4] and as a buffer layer for coated conductors [5–15]. Being a good refractory material, its recrystallization is not possible below 1500 °C. This makes it an efficient barrier of oxygen diffusion in high temperatures [13]. LZO as a buffer layer, is of particular interest in coated conductors because of its structural compatibility and excellent lattice match with $YBa_2Cu_3O_{7-x}$ (YBCO) (lattice parameter of LZO=10.79 Å) [15]. In the prevalent coated-conductor architecture, *c*-axis oriented YBCO layers are deposited on buffered Ni-based Rolling Assisted Biaxially Textured Substrates (RABiTS) [16,17]. The calculated pseudo-cubic lattice parameter of 3.81 Å of the LZO buffer layer, along the diagonal matching distance facilitates a low lattice mismatch to both YBCO and Ni-5%W substrates (0.5% and 1.8% mismatch to YBCO, *a*- and *b*-axes, respectively, and 7.6% to RABiTS Ni-5%W substrate) [15]. The LZO system has found its use as a single buffer layer replacing the first two layers of YSZ/CeO_2 in a traditional $CeO_2/YSZ/CeO_2$ buffer layer architecture on a Ni-5%W substrate [18]. Recently Paranthaman et al. [19] reported that, LZO layers can be grown over a wide compositional range by varying the percentages of lanthanum and zirconium according to the formulation $La_xZr_{1-x}O_y$. This has added to the benefit of choosing LZO as a buffer layer with possible adapted flexible compositions.

Since ceramic YBCO layers are deposited at high temperatures under oxygen atmosphere, oxidation of the Ni based substrate by O-diffusion and penetration of Ni-atoms into the superconducting layer can occur, which is problematic. Therefore, thick and epitaxial LZO buffer layers are needed in between the Ni based substrate and YBCO layer, in order to prevent any chemical interaction and diffusion that can occur between them. Paranthaman et al. [20] estimated the minimum thickness of the LZO layer for effective barrier action against Ni diffusion to be 75 nm, based on experimental studies using SIMS. Knoth et al. [21] based on XPS studies on thicker LZO buffer layers suggested a minimum requirement of 100 nm thickness. However, Caroff et al. [22] from their magneto-optical investigations determined a minimum thickness of 150 nm for a LZO layer in order to act as an efficient buffer layer with minimum transfer of defects from substrate onto the coated conductor. Furthermore, their work showed that a 250 nm thick film gave the highest critical current density (J_c).

Apart from thickness, a crystalline biaxial texture on the top surface of LZO layer is essential for passing on the epitaxy from the substrate to YBCO. This transfer of epitaxy is an important function of a buffer layer. The above discussed LZO layers prepared from non-water-based precursors exhibited good biaxial texture on their top surface. In our previous work based on water-based

precursors [23] it was reported that, a good quality LZO buffer layer with highly crystalline and biaxial textured top surface could be obtained up to a thickness of 40 nm. However, the barrier action of these films was insufficient to prevent Ni diffusion. Furthermore, single layer deposition of these layers at higher thicknesses (up to 100 nm), led to an increase in the FWHM values of biaxial orientation compared to that of the substrate (in-plane grain misalignment of 8.3° and out-of-plane grain misalignment of 9.2°, compared to the Ni-5%W values of 6.5° and 6.8°, respectively) and an amorphous top surface layers, as was shown from RHEED analysis. Inclusion of a seed layer of 20 nm thickness led to an improvised but yet, incompletely crystalline top surface [24].

This paper describes the possibility to grow thick LZO buffer layers from water-based solutions, with optimized crystallinity and epitaxial qualities for the textured growth of YBCO. Moreover, the appropriate chemical composition of the precursor solutions with additives (including polymer) for preparing thick LZO films, and their improvement in surface crystallinity with an inclusion of seed layer, are discussed in detail. To the best of the authors' knowledge, thick LZO layers prepared for coated conductor design with an inclusion of polymer in water-based precursor has not yet been reported in literature. In this work, epitaxial films prepared from chemical solution deposition (CSD) of LZO precursor solutions using water as the main solvent will be presented in follow-up to the previous reports using non-water-based solvents such as 2-methoxyethanol [20], propionic acid [21] and methanol [10,25]. In recent times, CSD is considered as one of the most promising techniques for the cost-effective processing of longer lengths of coated conductors [5–7,9–24]. CSD methods include the preparation and deposition of the precursor solution via one of the sol–gel routes, metal organic deposition (MOD) or hybrid routes using modifying ligands [26–28]. Since CSD employs a homogeneous distribution of metal ions in a solvent, the transfer of homogeneity from the as-deposited amorphous films to a crystalline film, can be ensured. Furthermore, CSD allows easy compositional adaptation and non-vacuum processing [27]. Additionally, water-based CSD preparation offers additional benefits of environmental friendliness, safe handling and cost reduction. It has been shown from previous studies that the water-based CSD method leads to environmentally, friendly and stable precursors needed for bulk materials and coatings for applications in the field of catalysis [29], materials with specific thermal expansion [30], drugs [31], buffer layers [23,24,32] and superconductors [33,34].

2. Materials and methods

2.1. Precursor solutions

Four different LZO precursor solutions were synthesized. Two of the four systems were prepared with inclusion of polymers. The compositional details of the precursor solutions are given below.

System 1: La acetate–Zr acetate hydroxide–EDA–EG system: A 0.4 mol/L LZO solution was prepared by dissolving zirconium acetate hydroxide ($Zr(CH_3COO)(OH)_3$, Aldrich) in water (molar ratio, $Zr^{4+}:H_2O=1:170$) at room temperature. Acetic acid was added to the metal ion solution (molar ratio, $Zr^{4+}:HOAc=1:20$) and the mixture heated to 80 °C. At 80 °C, lanthanum acetate ($La(CH_3COO)_3$ $1.5H_2O$, Alfa-Aesar, 99.9%) was added to the mixture (molar ratio, $La^{3+}:Zr^{4+}=1:1$) and stirred until clear. Ethylene–diamine tetra acetic acid (EDTA, Sigma-Aldrich, > 99.4%) was used as a complexing agent to keep the metals stable in solution at high concentrations and increased pH values [35,36]. The EDTA solution was prepared by dissolving EDTA in a

water and ethylene diamine (EDA, Fluka, 100%) mixture (molar ratio, $EDTA:H_2O:EDA=1:130:4$) at room temperature. The molar ratio of $EDTA:(La^{3+}+Zr^{4+})$ was fixed at 0.5:1. The metal ion solution was slowly added to the EDTA solution at room temperature and stirred for 10 min. The pH of the mixture was adjusted to 6 by adding ammonia [25% Ammonia solution, Carl Roth]. Subsequently, ethylene glycol (EG, Sigma-Aldrich, > 99%) was added at 60 °C (molar ratio, $EDTA:EG=1:4$). Excess solvent was evaporated until a concentration of ~ 0.4 mol/L was obtained. The pH of the final solution was found to be between 6.2 and 6.3 and the viscosity between 4.9 and 5.2 mPa s.

System 2: La acetate–Zr propoxide–EDA–EG system: A 0.4 mol/L LZO solution was prepared by dissolving stoichiometric lanthanum acetate in a water–acetic acid mixture (molar ratio, $La^{3+}:HOAc:H_2O=1:16:150$) at 80 °C until a clear solution was obtained. Here the zirconium precursor was changed to zirconium n-propoxide (70% w/w in n-propanol, Sigma-Aldrich). The water sensitivity of the zirconium alkoxide was reduced by stabilizing it with acetic acid (molar ratio, $Zr^{4+}:HOAc=1:4$) at room temperature [37]. The stabilized zirconium n-propoxide was diluted by adding water in a 1:20 molar ratio of $Zr^{4+}:H_2O$ at 80 °C. A clear solution was obtained after stirring for 5 min. at this temperature. This was followed by the addition of the zirconium precursor solution to the lanthanum precursor solution at 80 °C. The EDTA solution and the required amount of EG (molar ratio, $EDTA:EG=1:4$) were mixed with the metal ion solution ($La^{3+}+Zr^{4+}$) as described in system 1. Excess solvent was evaporated until the desired concentration of 0.4 mol/L was obtained. The final solution had a pH of 6.2–6.3 and a viscosity of 5.0–5.2 mPa s.

System 3: La acetate–Zr propoxide–EG–PVP system: System 3 is identical to system 2, except for addition of polyvinyl pyrrolidone (PVP, Alfa-Aesar, M.W. 8000) to the solution. After addition of EG, some amount of PVP was added (molar ratio, $(La^{3+}+Zr^{4+}):PVP=1:0.5$) and excess solvent was evaporated until a final concentration of 0.4 mol/L was attained. The pH and viscosity of the solution was found to be 6.3–6.4 and 5.5–5.8 mPa s, respectively.

System 4: La acetate–Zr propoxide–AMP–PVP system: The metal ion solution ($La^{3+}+Zr^{4+}$) was prepared as in system 2. An EDTA solution (molar ratio, $(La^{3+}+Zr^{4+}):EDTA=1:0.5$) was prepared by dissolving EDTA in water. The pH of this solution was increased by addition of ammonia until the EDTA was dissolved (pH between 7 and 8). Then, the metal ion solution ($La^{3+}+Zr^{4+}$) was slowly added to the EDTA solution at room temperature and stirred for 10 min. A viscous surfactant, 2-amino-2-methyl-1-propanol (AMP, Sigma-Aldrich, 95%) was added to the mixture (molar ratio, $EDTA:AMP=1:4$) to increase the wettability of this water-based precursor solution. The solution was heated to 60 °C. Finally, small amount of PVP (molar ratio, $(La^{3+}+Zr^{4+}): PVP=1:0.5$) was added and the final solution evaporated until the desired concentration was achieved. The pH of the solution was found to be 4.6–4.8 and the viscosity 4.6–4.9 mPa s. It was chosen to work at lower pH for system 4 because addition of the alkaline AMP at pH 6 caused uncontrolled gelation of the precursor and thus instability of the solution.

Table 1 summarizes the composition and the properties of the precursor systems 1–4.

2.2. Solution deposition and heat treatment

An alloyed RABiTS Ni-5%W was used as the substrate. 1 cm wide and 80 µm thick substrates (Evico, GmbH) were cut into strips of 2.5 cm length for dip-coating. The substrates were dip-coated in a clean room (class 10,000; flow cupboard class 100) in order to prevent contamination from dust particles. The humidity of the clean room was maintained anywhere between 44% and 49% and the temperature of the clean room was between 24 and 27 °C. The dip-coat speed was maintained between 40 mm/min and 60 mm/min.

Table 1
Composition and properties of the water-based precursor systems 1–4.

System	$[La^{3+}+Zr^{4+}]$ (mol/L)	Metal precursors	Solvent	Complexing agent	Additives	pH	Viscosity (mPa s)
1	0.4	La acetate, Zr acetate hydroxide	Water	EDTA	Acetic acid, EDA, EG, ammonia	6.2–6.3	4.9–5.2
2	0.4	La acetate, Zr propoxide	Water	EDTA	Acetic acid, EDA, EG, ammonia	6.2–6.3	5.0–5.2
3	0.4	La acetate, Zr propoxide	Water	EDTA	Acetic acid, EDA, EG, ammonia, PVP	6.3–6.4	5.5–5.8
4	0.4	La acetate, Zr propoxide	Water	EDTA	Acetic acid, AMP, ammonia, PVP	4.6–4.8	4.6–4.9

The as-deposited wet layers were transformed into a gel by placing them in a drying furnace at 60 °C for one hour. The amorphous layers in their gel state were subjected to a suitable heat treatment to create the desired crystalline metal oxide phase, in the following sequence: Firstly, the layers were heated from room temperature to 450 °C (ramp rate of 1 °C/min) and let to dwell for one hour. Secondly, a 3 °C/min heating ramp was applied from 450 °C to 900 °C (dwell time=1 h). Finally, the films were heated to 1050 °C at a 10 °C/min ramp with a dwell time of one hour. After the heat treatment, the furnace was switched off and the samples were left to cool inside the furnace. The entire heating process was carried out in an Ar-5%H_2 atmosphere (gas flow rate: 0.55 L/min).

2.3. Characterization

The thickness of the crystallized layers was analyzed by spectroscopic ellipsometry (J. A. Woollam Co) and by fitting the experimental curve to the model for LZO films on Ni-5%W substrates (wavelength=638.3 nm and refractive index=1.998). The crystallinity of the film was analyzed using a standard X-ray diffractometer (Siemens D 5000). A Bruker, AXS Discoverer diffractometer was used to measure the pole-figures and phi scans. Analysis of the microstructure of the surface was performed with the help of a scanning electron microscope (FEG-SEM, FEI). The crystallinity of the top surface was verified using reflection high energy electron diffraction (RHEED, Staib instruments) with an energy of 30 keV at an incidence angle of 1–2°. Investigation of the detailed microstructure was performed in a C_s-corrected transmission electron microscope (TEM, JEOL 2200 FS). For preparing the TEM samples, an in-situ lift-out procedure (FEI, Nova 600 Nanolab dual-beam FIB) was made use of. The surface roughness of the layers were characterized using an atomic force microscope (AFM, Molecular Imaging Picoplus with Picoscan 2100 controller) in tapping mode. The buffer layer action was evaluated by means of monitoring the Ni penetration depth using X-ray Photoelectron Spectroscopy (S-Probe monochromatized XPS spectrometer, Surface Science Instruments (VG)), using an Al-$K\alpha$ source (monochromatized Al-radiation: 1486.6 eV), at a base pressure of 2×10^{-9} mbar and an acceptance area of 250×1000 μm^2, with an hemispherical analyzer at a pass energy of 157.7 eV. The measured surface was 250 μm by 1000 μm. The voltage of the Ar$^+$-ion gun was maintained at 4 keV to sputter an area of 3×3 mm^2. Experimental data were processed using the software package CasaXPS (Casa Software Ltd., UK) using Shirley background and Scoffield sensitivity factors.

3. Results and discussion

3.1. Solution stability, complexation and polymer addition

3.1.1. Stability of alkoxides against hydrolysis

In systems 2–4, the zirconium propoxide was stabilized by mixing it with acetic acid in order to handle it in non-vacuum and water-based conditions. Acetic acid partially replaces the propoxide

(OPr) groups by acetate groups (OAc) forming a zirconium propoxide–acetate complex that reduces the chances of immediate hydrolysis and condensation reaction of zirconium propoxide on addition of water [37].

3.1.2. Complexation, viscosity and wettability

In all the systems, EDTA was used as a strong chelating agent. It can form complexes with both lanthanum and zirconium ions [36], avoiding the metal ions from precipitating when high metal concentrations are reached during the transformation from solution to gel and finally to the solid state. The solubility of EDTA in water increases with increasing pH [38]. Therefore, EDA was used as a pH increasing alkaline substance to initially increase the pH of water to dissolve EDTA. Based on the previous studies of EDTA complexation with Ce^{3+}, it was inferred that EDTA forms stable complexes with Ce-metal ions leading to a stable solution at a pH between 5.5 and 6 [35]. Hence, applying the same principle ammonia was added to the EDTA-metal ion solution mixture to adjust the pH to 6 in systems 1–3, which were prepared under comparable conditions. Ammonia was chosen instead of EDA to adjust the pH in order to keep the organics to a minimum. It is believed that, similar to the formation of a polymeric species by the reaction of citric acid and EG in a Pechini process [26], EDTA, being a polyamino carboxylic acid reacts with EG and results in the formation of polymeric species. The resulting polymeric species can increase the viscosity of the solution. Therefore, EG was used in systems 1–3 to increase the viscosity of the solutions and subsequently their wettability on the metallic substrates. AMP, which is a surfactant that is highly alkaline in nature was used in system 4. It reduces the surface tension of the water-based precursor solution and increases the pH of the solution. In system 4, AMP therefore replaces EDA (for its high alkalinity) and EG (for wettability and viscosity increase) used in system 1–3.

3.1.3. Polymer addition

PVP was added to systems 3 and 4 in order to increase the maximum single layer thickness for crack-free films. PVP is considered to promote structural relaxation during the heat-up stage of the annealing treatment thereby causing a reduction in stress during the formation of the layer and thus suppressing crack formation [39]. PVP can promote an increase in the viscosity of the solution [40]. This is evident in system 3 in comparison to systems 1 and 2. Since only a very small amount of PVP was added (0.555 g in 25 ml of precursor solution), a small increase in viscosity was observed.

3.2. Crystallinity and orientation

In order to study the epitaxial growth and crystallinity of the LZO buffer layers, XRD analysis were performed on the layers prepared from the four systems and comparisons were made. For systems 1 and 2, crack-free LZO layers of 100–120 nm thicknesses were obtained at a dip-coating speed of 40 mm/min. For systems 3 and 4, crack free layers of 280 and 140 nm thickness,

respectively, could be obtained with an increased dip-coating speed of 60 mm/min. The maximum crack-free thickness obtained for these layers has been considered for the studies. This increase in thickness of the layer, made from system 3 compared to system 4, will be discussed in detail in Section 3.3. Fig. 1 shows the X-ray $\theta-2\theta$ scans of the LZO layers obtained from systems 1–4 (S1–S4). The reflections were indexed based on the pyrochlore lattice cell of LZO with a lattice parameter of $a_{LZO}=10.79$ Å. The epitaxial c-axis oriented (0 0 l) reflections of LZO could be observed in the range of 0°–80° with the (0 0 4) peak position at $2\theta=33.3°$ and the less intense (0 0 8) peak position at $2\theta=69.83$. A very small undesired peak of (2 2 2) orientation was also observed at the peak position of $2\theta=28.6°$. It is clear from the figure that for all the samples, the (0 0 4) LZO reflection appears to be the most intense one. The preferential c-axis growth can be quantified by calculating the peak intensity ratio values defined as in Eq. (1) [8].

$$\text{Peak intensity ratio} = \frac{I_{\max(0\,0\,4)}}{[I_{\max(0\,0\,4)}+I_{\max(2\,2\,2)}]}100\% \qquad (1)$$

$I_{max(004)}$ and $I_{max(222)}$ are the maximum intensity of the (0 0 4) and (2 2 2) peaks, respectively. From the I_{max} values obtained from Fig. 1, peak intensity ratios of 95.10%, 92.30%, 88.88%, and 95.05% were obtained for systems 1–4 (S1–S4), respectively. Layers obtained from S1 and S4 show peak intensity ratios above 95%. This indicates that epitaxial and c-axis oriented LZO layers were obtained. From the lower peak intensity ratio value for S3, it can be concluded that this system leads to less preferential c-axis growth.

Additionally, the absolute peak intensities of the (0 0 4) reflection related to the thickness of the film show values of 274 counts for a 280 nm thick film for S3, while a higher value of 396 counts for a 110 nm thick film was obtained for S2. Based on the intensity of the peaks and their respective thicknesses, it can be concluded that the absolute crystallinity of S3 is lower, although both samples have the same composition, except for PVP addition in S3.

Fig. 2(a) and (b) represent the pole-figures of the Ni-5%W substrate compared to that of the LZO layer for system 4. Fig. 2(c) represents the phi-scans carried out to measure the in-plane grain misalignment of the (2 2 2) plane of the four LZO layers made from systems 1–4 (S1–S4). From the figures it can be seen that the LZO layers have clearly grown with a 45° rotation on
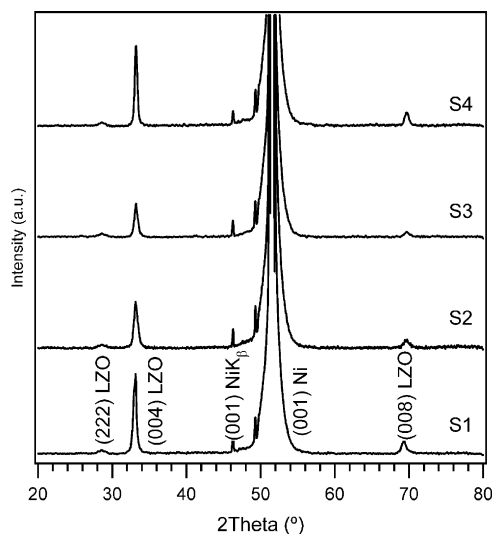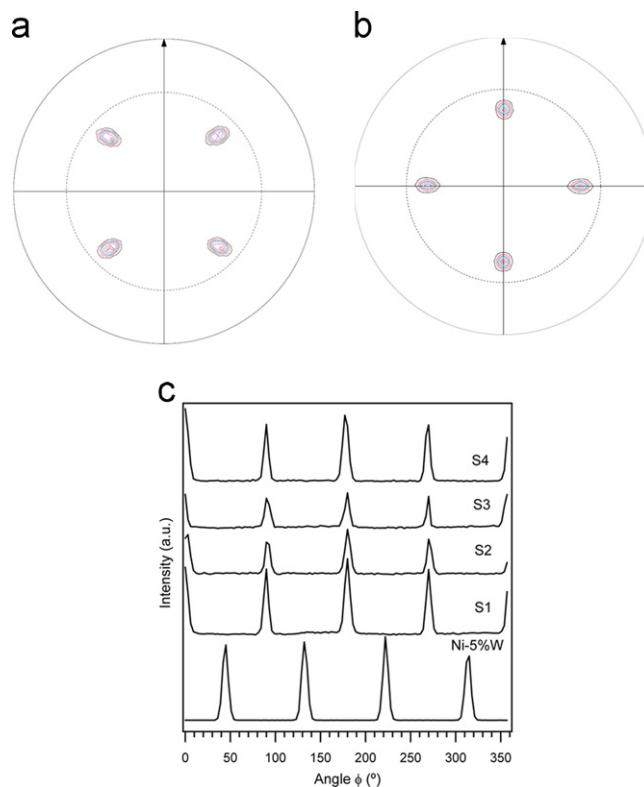

Fig. 2. (a) Pole-figure of Ni-5%W substrate and (b) LZO layer from system 4 deposited on top of Ni-5%W substrate; and (c) X-ray Φ-scan patterns of LZO films on Ni-5%W substrates, prepared from precursor systems 1–4, denoted as, S1–S4, at $2\theta=28.62°$ and $\Psi=54.00°$.

top of the Ni-5%W substrate. The average full width at half maximum (FWHM) of the reflections for LZO layers corresponding to systems 1, 2, 3 and 4 were found to be 6.12°, 6.85°, 6.67° and 6.59°, respectively. These values are very close to the FWHM of 6.10° of the Ni-5%W substrate, which indicates that the biaxial texture from the substrate was successfully transferred to the LZO layers. Layers made from systems 1 and 4 show the highest intensities as was observed in the X-ray $\theta-2\theta$ results. The FWHM values of the peaks for all the above tested layers are comparable to the values reported for that of the LZO layers from non-water-based MOD systems (6.5° [12] and 6.90° [15]), the LZO films from vacuum based pulsed laser deposition (PLD) system (6.2° [8]) and the water-based LZO films of 40 nm thickness (6.65° [23]).

The out-of-plane orientation of the LZO layers on top of the Ni-5%W substrate was determined by rocking curve measurements along the (0 0 4) plane of LZO. The results are depicted in Fig. 3. The FWHM of the peaks of the LZO layers obtained from systems 1 to 4 (S1–S4) were found to be 7.20°, 7.20°, 7.08° and 7.42°, respectively. These values are comparable to that of the non-water-based MOD LZO thin films (7.20° [15]) and the PLD based LZO films (7.30° [8]). In the earlier work on water-based LZO film of 40 nm thickness, a higher FWHM value of 8.80° was reported [23].

A crucial parameter that determines the quality of a good LZO buffer layer is the transfer of texture from the substrate to the outer surface of the buffer layer. Perfect crystallinity and orientation of the buffer layer surface is a prerequisite for high quality YBCO growth on top. Therefore, the quality of the top surface of the LZO layers obtained from the different precursor systems was verified by performing RHEED analysis. Fig. 4 shows the RHEED patterns for LZO layers on Ni-5%W substrate obtained from the four different precursor systems (S1–S4). Despite the good in- and out-of-plane grain misalignment seen in Figs. 2(c) and 3, all four

Fig. 1. X-ray $\theta-2\theta$ diffraction patterns of LZO films on Ni-5%W substrates, prepared from precursor systems 1–4, denoted as, S1–S4.

systems show ring like patterns in the RHEED analysis. This implies that the top surfaces of the layers are polycrystalline or randomly textured. There are some discrete spots (marked by circles and arrows) inside the ring like pattern for S1 and S4, suggesting a small percentage of biaxial texture which signifies the presence of (0 0 2) oriented top surface. Therefore, it can be concluded that further improvement in the top surface crystallinity of the LZO films is necessary to promote the growth of well-textured, c-axis oriented YBCO layer. The improvement in the top surface crystallinity will be discussed in Section 3.5.

3.3. Microscopy analysis

A dense surface morphology is essential for a buffer layer in order to prevent the diffusion of nickel atoms into the YBCO layers as well as the oxidation of the Ni-5%W substrate that takes places during physical deposition of YBCO or during heat-treatment of CSD YBCO layers. Therefore, SEM analyses were performed to understand the morphology of the top surface of the layers made from all the four systems. Fig. 5 displays the SEM micrographs of the different LZO layers. As seen from the figure, LZO layers obtained from systems 1, 2 and 4 (S1, S2 and S4) show an almost identical, dense surface morphology. However, the LZO layer obtained from system 3 (S3) is clearly porous which is undesirable for a good buffer layer. The main reason for this porosity can be attributed to the burn-out of the polymeric PVP. The formation of the pores can be seen as a suppression mechanism for the otherwise formation of large cracks for stress-relief, and thus a possibility of thickness enhancement in the metal oxide films [39–42]. Nevertheless, Kozuka and Higuchi
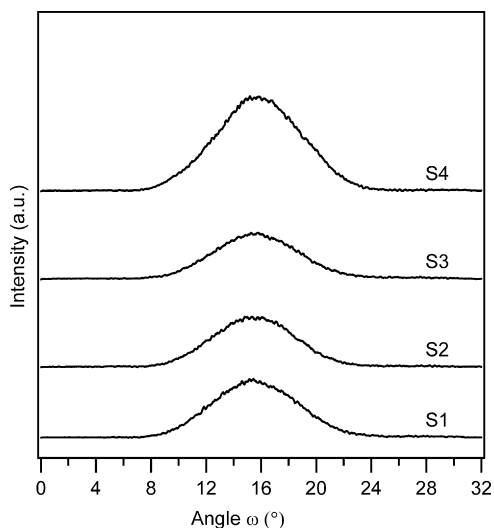
[39] had mentioned the advantage of pyrolysis under a slow heating rate as a means to avoid the undesired appearance of large pores in the metal-oxide films containing PVP. Although the layers from all the four systems had been treated under slow heating ramp during the pyrolysis step, the undesired porous surface morphology is witnessed only in the LZO layer prepared from system 3. Moreover, despite having an equal molar ratio of polymeric PVP, an entirely different morphology can be seen under SEM for the layers made from systems 3 and 4 (S3, S4).

As a reasoning behind the pore formation seen in the LZO layers from system 3, it can be stated that in the solution state of system 3, EDTA-EDA-EG-PVP forms a longer length polymeric chain compared to that of EDTA-AMP-PVP in system 4. Therefore, during the burn-out of this long length polymeric chain, large pores can be formed throughout the amorphous layer. These pores can only be intermittently filled alongside the crystallization and growth of metal-oxide at higher annealing temperatures. These incompletely filled void spaces are spread throughout the length and breadth of the LZO layer, which results in a puffed-up layer with dispersed LZO grains among the void spaces, exhibiting high thicknesses. This explains the increased crack-free thickness of LZO layer prepared from system 3 (280 nm) in comparison to system 4 (140 nm), although dip-coated at the same withdrawal speed of 60 mm/min. Additionally, in order to check if the LZO layers showed an increased porous morphology with a higher amount of PVP, a molar ratio of EDTA:PVP=1:1 was used in systems 3 and 4. In this case, thick, single layer LZO films of 280 nm with porous morphology (system 3) and 260 nm with denser morphology (system 4) were obtained at a withdrawal speed of 40 and 80 mm/min, respectively. From the above discussion it can be concluded that, in combination with the polymeric PVP, the use of AMP in system 4 replacing the EDA and EG used in system 3 has been beneficial. It has led to a precursor system, where stress relief in the layer with an increased thickness can be obtained, without resulting in a negative effect of exaggerated pore formation. Chemically, AMP is a sterically hindered form of monoethanolamine (MEA) [43]. It's role as an alkaline medium and a wetting agent, replacing EDA and EG of system 3, has helped minimizing the formation of long length polymeric chain in the solution state, in spite of the presence of PVP. Hence, the pyrolysis of LZO film from system 4 has resulted in smaller pores compared to that of LZO film from system 3, that can easily be filled-up during the crystallization and metal-oxide growth at higher temperatures, and lead to a denser surface morphology.

Layers from systems 2 and 4 were chosen for TEM cross-sectional analysis in order to investigate, in nanoscale, their structure. Since both the systems were made using the same metal precursors (La acetate and Zr propoxide) and the layers from these systems possess a dense surface morphology, the study is deemed to be relevant for the investigation. Fig. 6 shows the TEM images for LZO layers from system 2 and 4. From the figure, it can be seen that the images contain many brighter regions apart from the darker ones. In literatures, these bright

Fig. 3. Rocking curve measurements along the (0 0 4) plane of the LZO films on Ni-5%W substrates, prepared from precursor systems 1–4, denoted as, S1–S4.
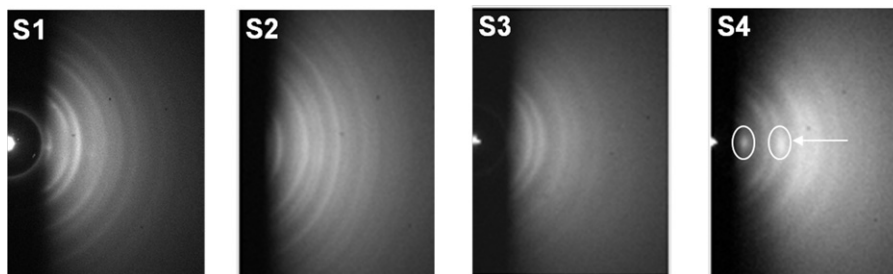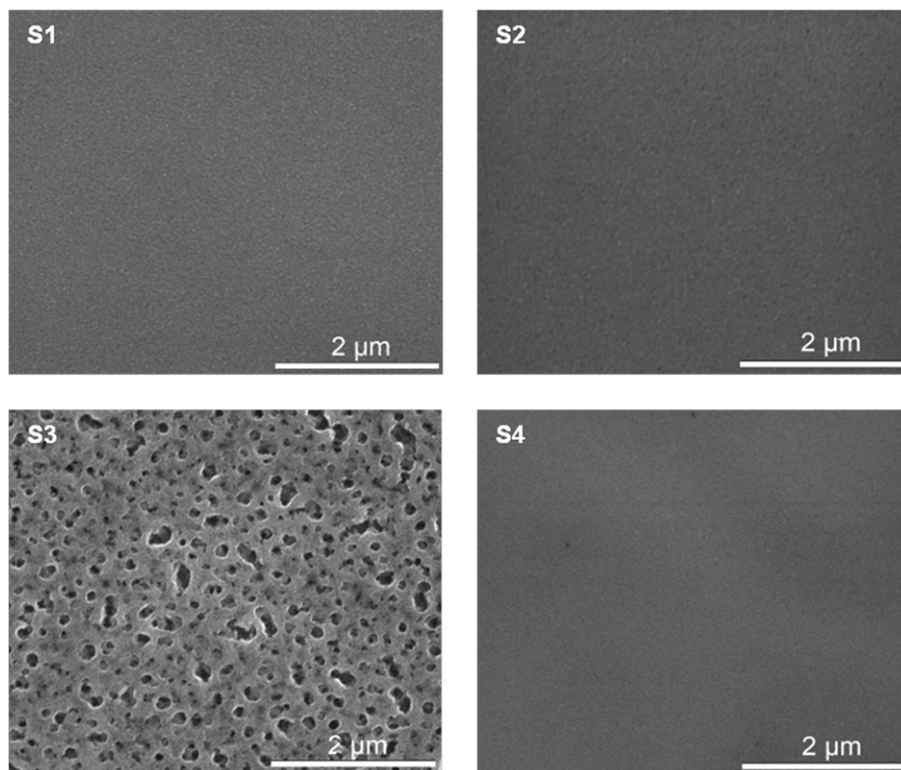
Fig. 4. ⟨0 0 1⟩ RHEED patterns of the LZO layers on Ni-5%W substrates, prepared from the precursor systems 1–4, denoted as, S1–S4.

Fig. 5. SEM images of the LZO layers on Ni-5%W substrates prepared from precursor systems 1–4, denoted as S1–S4, at a magnification of 50 K.
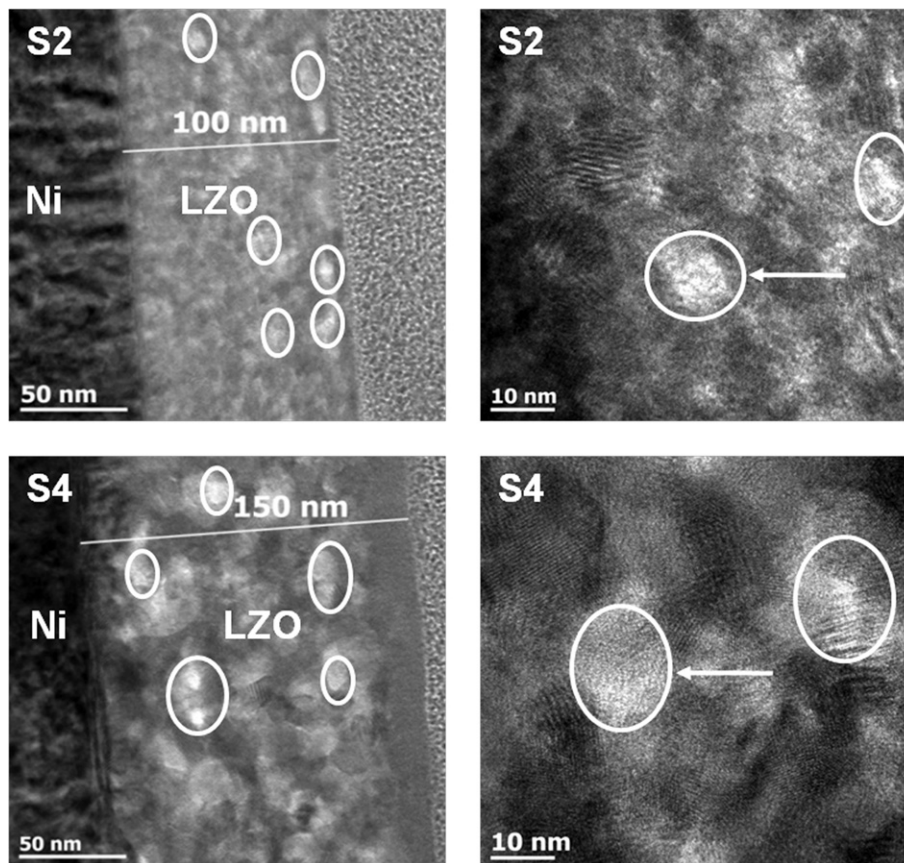

Fig. 6. TEM cross-sectional overview of the LZO layers depostied on Ni-5%W substrate prepared from system 2 (S2) and system 4 (S4) seen under different magnifications. TEM samples prepared using FIB lift-off method.

regions are termed as nanovoids [24,44,45]. Since they are lesser in density compared to the neighboring LZO grains, they are seen brighter in the image contrast of TEM. Therefore, it can be inferred that the bulk of the layers from both the systems contain nanovoids, although their corresponding top surfaces appeared denser in the SEM-analysis (Fig. 5). The size of the nanovoids was found to be in the range of 10–20 nm. These sizes are in agreement with that of the nanovoids reported in literature [44,45]. Molina et al. [44] have done extensive TEM analysis on these nanovoids and concluded that they were initially filled with carbon-rich gases formed during pyrolysis. In the work of Jiménez et al. [45], it was observed that the nanovoids were formed even in the amorphous state at 500 °C. Apparently, these voids did not affect the final crystalline state of the layer formed at 960 °C and did not contain anymore carbon. Cloet et al. [24] described that, the use of reducing atmosphere (Ar-5%H_2) seriously hampers the perfect growth of dense LZO layers, which results in the occurrence of nanovoids.

The nanovoids as seen from Fig. 6, are homogeneously distributed throughout the bulk of the layer until near the surface. This is prominent for the layer from system 4 (S4) than that from system 2 (S2) where the top ~15% of the layer was free from nanovoids. This is in line with the observations of Cloet et al. [24]. However, this dense structure near the surface can comprise partly of trapped or incompletely expelled carbon during pyrolysis which is undesirable for the surface texture. This analysis on the presence of carbon in the layers is a part of the discussion in Section 3.4.

Since it is absolutely necessary to create buffer layers with a smooth, low roughness surface in order to be able to obtain high quality YBCO growth on top, AFM analysis was performed on all of these layers as shown in Fig. 7. It is found that replacing zirconium acetate hydroxide with zirconium n-propoxide decreases the root mean square (RMS) roughness over 25 μm^2 from 3.95 nm in system

1 (S1) to 2.15 nm in system 2 (S2) [46]. These RMS values are in line with the results obtained for MOD–LZO buffer layers [14]. Yet, system 2 it is found that, in spite of the low RMS values, larger particles are present on top of the low roughness layer, which can be detrimental for futher YBCO deposition. In line with SEM results, AFM images for an LZO layer deposited from system 3 (S3) reveals the presence of a high number of pores and a high RMS roughness of 12.70 nm. Yet, when combining this PVP with AMP in system 4 (S4), this porosity can be avoided and a dense LZO layer with an RMS roughness of 3.81 nm was obtained. All the RMS roughness values were found to be lower in comparison to that of the earlier water-based LZO layer (8.66 nm [23]). Since, a smooth buffer layer surface is preferred for the YBCO deposition, from the AFM measurements it can be concluded that, system 4 is the most suited for creating smooth buffer layer surface.

3.4. Buffer layer action: XPS study

The buffer layer action against Ni penetration of an LZO layer of 110 nm thickness and 140–150 nm thickness obtained from system 2 and 4, respectively, was studied by performing an XPS depth profile analysis. The LZO layers were subjected to 50 s of Ar^+ ion bombardment for 20 cycles. Fig. 8(a) and (b) shows the results of the consecutive sputter cycles for the LZO layers obtained from system 2 and 4, respectively. The relative elemental occurrence of La, Zr, Ni, W, C and O after each sputter step is shown. Although the metal ion ratio of La:Zr in the solutions (systems 1–4) was maintained as 1:1, it is evident from the figures that there is a difference in the sputtered rate of Zr in comparison to La during Ar^+ ion bombardment in both the samples. This is in line with the observation of Knoth et al. [15]. They reported that during sputtering, the localized structural
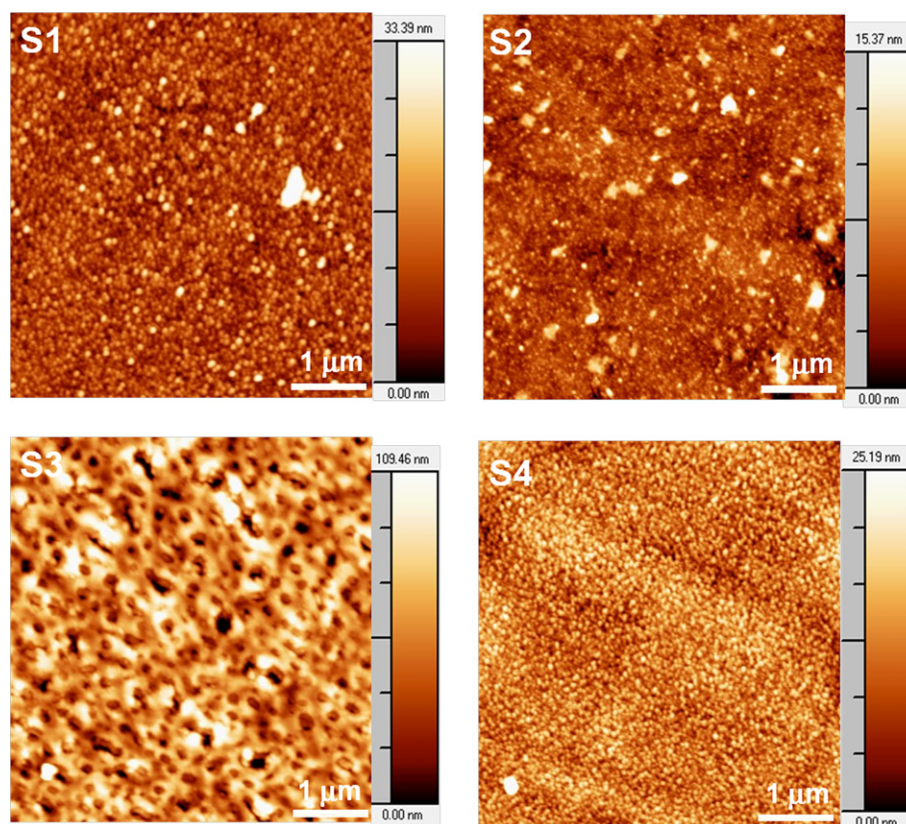

Fig. 7. AFM microscopy images (scanning area 5 × 5 μm^2) obtained for LZO layers deposited from precursor systems 1–4, denoted as S1–S4.
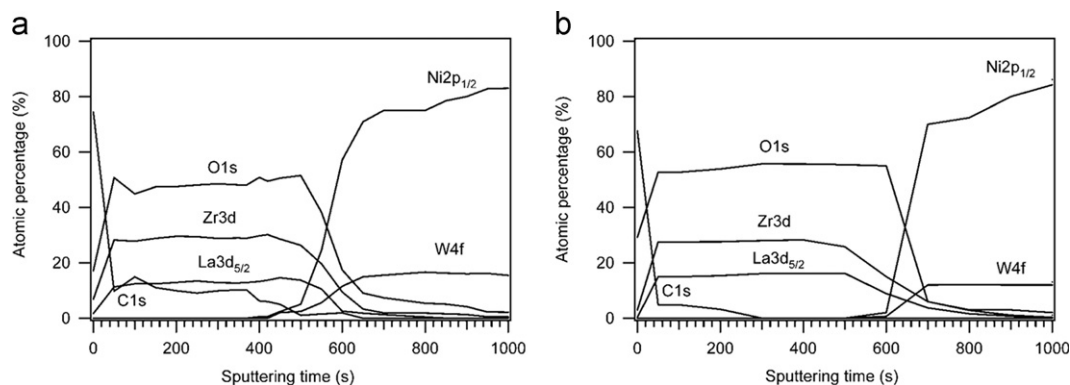
Fig. 8. XPS depth profile analysis plots on buffer layer action of LZO layer on top of Ni-5%W substrate prepared from (a) system 2 and (b) system 4.

differences and defects within the thin layers gave rise to the stronger decomposition of the oxidic Zr bonding that result in the difference. Based on this it can be understood that, the percentage of Zr compared to that of La and O is overestimated.

From Fig. 8(a) it can be observed that for the LZO layer prepared from system 2, carbon contamination (> 5%) is present throughout bulk of the layer until the occurrence of Ni that was seen after 450 s of sputtering. However, for the layer from system 4 (Fig. 8(b)), the presence of carbon inside the layer ($\sim$5%) is seen only until the layer thickness corresponding to the first 100 s of sputtering. The composition of the top layers for both the samples before sputtering can be neglected because of the surface contamination with environmental carbon. Following this, correlations between the TEM images (Fig. 6) and the XPS plots (Fig. 8(a) and (b)) corresponding to the two systems can be made. XPS plots show that the bulk of the LZO layer from system 2 contain lot more carbon than that of system 4. This implies that, the darker regions visible in the corresponding TEM images amongst the nanovoids in the bulk of system 2 can be a mixture of the LZO grains and the remaining amount of unexpelled carbon that was formed during pyrolysis (Fig. 6). On the other hand it is clear from Fig. 8(b) that nearly all the carbon except for the near top surface is absent for the layer made from system 4 ($\sim$100 s of sputtering). On correlating this information to that of the TEM images for the layer from system 4 (Fig. 6) it can be understood that, the dark and nanovoid-free region near the top surface is a dispersion of the entrapped carbon among the LZO grains. The presence of carbon only near the top surface of the LZO layer from system 4 signifies that, some amount of carbon is partially trapped near the top surface during its removal from the bulk of the layer. Presence of unexpelled carbon in the bulk of the layer can be detrimental during the epitaxial growth of oriented buffer layers. Knoth et al. [15] in their work reported the presence of a mere 0.6% of carbon in their LZO layers prepared by non-aqueous route with optimal qualities. The lower amount of trapped carbon in the layer from system 4 can also be considered as a reason for its better crystalline qualities compared to the layer from system 2 (see Section 3.2). This strengthens the interest of selecting system 4 for further investigation. As seen in Fig. 8(b), the percentage of La and Zr decreased to half its maximum and the Ni increased towards its half maximum after $\sim$700 s of sputtering. Based on this and the estimated thickness of 140–150 nm (system 4) from ellipsometry and TEM, the sputtering rate was estimated to be 2.0 Å/s (including estimated error). From Fig. 8(b), it is seen that the first traces of nickel are found after 550 s of sputtering. Based on the estimated sputter rate, it can be inferred that the Ni penetration was restricted to the first 30 nm of the 140–150 nm thick layer. This implies that the LZO layer prepared from system 4 acts as an effective buffer layer.

3.5. Surface texture improvement of the thick LZO layer

Optimum thickness of the layer and a high crystallinity of the top surface are the two requisites for a good buffer layer. Thickness of the layer should be high enough to prevent inter-diffusion of O and Ni and, a high crystallinity of the top surface is required to ensure transfer of texture to the YBCO layer grown on top. Attempts were made to further improve the top surface (2–5 nm) crystallinity. LZO layers from system 4 were considered for further improvement as it gave the best results according to the combination of results obtained from XRD, SEM, TEM and XPS (Sections 3.2–3.4). As an initial attempt, variations in the rates of gas flow and heat treatment were made. The gas flow rate during the heat treatment was decreased to $\sim$20% of its original value, considering that, the reducing gas can be detrimental for the oxide formation. The heating ramp was increased to 10 °C/min while heating directly from room temperature until the final crystallization temperature of 1050 °C, taking into account that higher ramp rates can avoid the formation of undesired but thermodynamically stable (2 2 2) phase. On the contrary, neither the decrease in gas flow rate nor the increase in heating rate led to any significant improvement in the top surface texture. The surface texture remained similar to the RHEED pattern observed in Fig. 4.

Following the previous attempts, seed layers were incorporated into the thick layers in an effort to improve the surface crystallinity. A seed layer of a few nanometers thickness had been used by several researchers to improve the crystallinity and epitaxial growth of the oriented layers [24,47–50]. A thin seed layer on a textured substrate possesses a low interfacial energy, as their unstacked grains grow as isolated islands which can act as nucleation sites. Subsequent deposition of a thicker layer onto this nucleation sites can result in the growth of a highly oriented film [47]. Seed layer of 15 nm thickness was deposited on the Ni-5%W substrates from LZO precursor solutions of 0.2 M concentration at a withdrawal speed of 30 mm/min [24]. The heat-treatment was carried out as per that of the thick layer at a gas flow rate of 0.1 L/min. This was followed by the usual deposition of the 140 nm thick films prepared from system 4. The final thickness of the layer after the deposition of the 140 nm thick film was found to be $\sim$155 nm. This layer showed significant improvement in its epitaxial growth and surface crystallinity.

The X-ray analysis carried out on the LZO buffer layer with the additional seed layer are shown in Fig. 9(a) and (b). The X-ray $\theta - 2\theta$ scan (Fig. 9(a)) reveals an exceptionally highly textured LZO growth oriented along the (0 0 4) plane, which is thrice as high in counts in comparison to LZO film without a seed layer. The (0 0 4) oriented peak intensity ratio of the improved LZO layer was found to be 97.50%. From the phi-scan (Fig. 9(b)), the FWHM of the in-plane
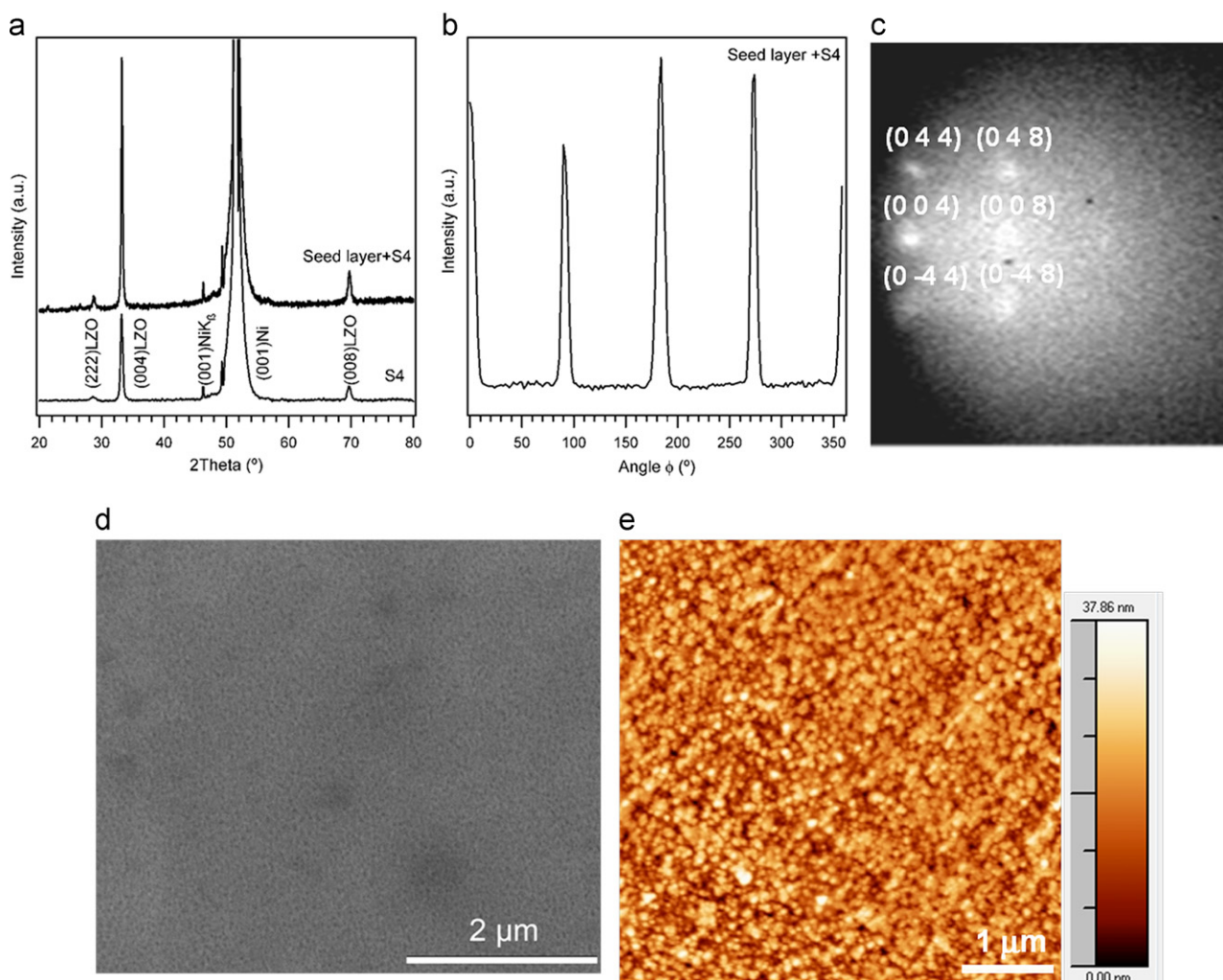
Fig. 9. (a) X-ray $\theta - 2\theta$ diffraction patterns of the LZO films, prepared from precursor system 4, with and without an additional seed layer on Ni-5%W substrates; (b) X-ray Φ-scan pattern for LZO film, prepared from precursor system 4, with an additional seed layer on Ni-5%W substrates; (c) $\langle 0\,0\,1 \rangle$ RHEED pattern for the same LZO layer; (d) SEM image and (e) AFM image of the LZO layer prepared with a seed layer on Ni-5%W substrates.

grain misalignment was found to be 6.60°, which signifies the good epitaxial growth and crystallinity. The RHEED pattern of the improved LZO layer shows distinct spots (Fig. 9(c)). This spotted pattern confirms the presence of a significant amount of crystalline top surface on the layer and effective transfer of biaxial texture from the substrate to the buffer layer. From the above results it can be concluded that, incorporation of the seed layers promoted a significantly high epitaxial growth of the thick LZO layer along the desired (0 0 4) plane. This increment in the (0 0 4) LZO grain orientation in comparison to that of (2 2 2) has resulted in good surface crystallinity that is evident as discrete spots, which corresponds to the biaxial texture in the RHEED analysis. Fig. 9(d) shows the SEM image of this improved LZO layer. It can be seen that the surface of the layer was crack-free and dense. From AFM analysis, the RMS roughness value over 25 μm^2 was found to be 5.80 nm (Fig. 9(e)). This increment in surface roughness for double layer deposition of LZO has been previously reported by Knoth et al. [21].

4. Conclusion

This research work presents a series of chemical solution deposition routes suited for the preparation of thick, crack-free LZO films from water-based precursors. Three of the four precursor formulations result in thick (100–140 nm), single layer

films with dense morphology and epitaxial growth. Their in-plane and out-of-plane grain misalignment are comparable to that of non-water-based CSD and PLD LZO films.

The addition of a polymer was beneficial in increasing the single layer thickness, but it also created a porous surface in one of the formulations. The pores created in the layers are found to be inter-dependent on the total chemical composition of the solution and not on the mere presence of the specific polymer. The TEM studies revealed the presence of nanovoids in the layers, which is inherent to all LZO films.

The best LZO layer acted as a good barrier against Ni penetration. A seed layer was incorporated in order to improve the crystallinity of the top surface of the LZO layer to support the growth of textured YBCO. Finally, a thick and high quality LZO layer from the water-based precursor solution, with improved biaxial texture on the top surface was obtained.

measurements and Michael Bäcker (Zenergy Power, GmbH) for providing Ni-5%W tapes.

References

[1] J.Y. Li, H. Dai, Q. Li, X.H. Zhong, X.F. Ma, J. Meng, X.Q. Cao, Mater. Sci. Eng. B—Solid 133 (2006) 209–212.

[2] G. Suresh, G. Seenivasan, M.V. Krishnaiah, P.S. Murti, J. Nucl. Mater. 249 (1997) 259–261.

[3] H. Chen, Y. Gao, S. Tao, Y. Liu, H. Luo, J. Alloy. Compd. 486 (2009) 391–399.

[4] X.Q. Cao, R. Vassen, W. Jungen, S. Schwatrz, F. Tietz, D. Stöver, J. Am. Ceram. Soc. 84 (2001) 2086–2090.

[5] T.G. Chirayil, M.P. Paranthaman, D.B. Beach, D.F. Lee, A. Goyal, R.K. Williams, X. Cui, D.M. Kroeger, R. Feenstra, D.T. Verebelyi, D.K. Christen, Phys. C: Supercond. 336 (2000) 63–69.

[6] M.P. Paranthaman, S. Sathyamurthy, L. Heatherly, P.M. Martin, A. Goyal, T. Kodenkandath, X. Li, C.L.H. Thieme, M.W. Rupich, Phys. C: Supercond. 445–448 (2006) 529–532.

[7] S. Sathyamurthy, M.P. Paranthaman, H.Y. Zhai, S. Kang, H.M. Christen, C. Cantoni, A. Goyal, P.M. Martin, IEEE Trans. Appl. Supercond. 13 (2003) 2658–2660.

[8] L.L. Ying, Z.Y. Liu, Y.M. Lu, B. Gao, F. Fan, J.L. Liu, C.B. Cai, T. Thersleff, S. Engel, R. Hühne, B. Holzapfel, Phys. C Supercond. 469 (2009) 288–292.

[9] M.P. Paranthaman, S. Sathyamurthy, M.S. Bhuiyan, A. Goyal, T. Kodenkandath, X. Li, W. Zhang, C.L.H. Thieme, U. Schoop, D.T. Verebelyi, M.W. Rupich, IEEE Trans. Appl. Supercond. 15 (2005) 2632–2634.

[10] H.S. Chen, R.V. Kumar, B.A. Glowacki, Mater. Chem. Phys. 122 (2010) 305–310.

[11] Z. Yu, P. Odier, S. Morlens, P. Chaudouët, M. Bacia, L. Zhou, P. Zhang, L. Jin, C. Li, P. David, O. Fruchart, Y. Lu, J. Sol-Gel Sci. Technol. 54 (2010) 363–370.

[12] Y. Wang, L. Zhou, Y. Lu, C. Li, Z. Yu, J. Li, L. Jin, Y. Zhang, Y. Shen, J. Mater. Sci.-Mater. El 22 (2011) 474–480.

[13] T. Caroff, S. Morlens, A. Abrutis, M. Decroux, P. Chaudouët, L. Porcar, Z. Saltyte, C. Jiménez, P. Odier, F. Weiss, Superconductor. Sci. Technol. 21 (2008) 075007.

[14] K. Knoth, R. Hühne, S. Oswald, L. Schultz, B. Holzapfel, Superconductor Sci. Technol. 18 (2005) 334–339.

[15] K. Knoth, R. Hühne, S. Oswald, L. Schultz, B. Holzapfel, Acta Mater. 55 (2007) 517–529.

[16] A. Goyal, D.P. Norton, D.K. Christen, E.D. Specht, M.P. Paranthaman, D.M. Kroeger, J.D. Budai, Q. He, F.A. List, R. Feenstra, H.R. Kerchner, D.F. Lee, E. Hatfield, P.M. Martin, J. Mathis, C. Park, Appl. Supercond. 4 (1996) 403–427.

[17] A. Goyal, F.A. List, J. Mathis, M.P. Paranthaman, E.D. Specht, D.P. Norton, C. Park, D.F. Lee, D.M. Kroeger, D.K. Christen, J.D. Budai, P.M. Martin, J. Supercond. 11 (1998) 481–487.

[18] Z. Liu, S. Wang, S. Zhao, Y. Zhou, J. Supercond. Nov. Magn. 18 (2005) 537–540.

[19] M.P. Paranthaman, S. Sathyamurthy, X. Li, E.D. Specht, S.H. Wee, C. Cantoni, A. Goyal, M.W. Rupich, Phys. C: Supercond. 470 (2010) 352–356.

[20] M.P. Paranthaman, S. Sathyamurthy, M.S. Bhuiyan, P.M. Martin, T. Aytug, K. Kim, M. Fayek, K.J. Leonard, J. Li, A. Goyal, T. Kodenkandath, X. Li, W. Zhang, M.W. Rupich, IEEE Trans. Appl. Supercond. 17 (2007) 3332–3335.

[21] K. Knoth, R. Hühne, S. Oswald, L. Molina, O. Eibl, L. Schultz, B. Holzapfel, Thin Solid Films 516 (2008) 2099–2108.

[22] T. Caroff, L. Porcar, P. Chaudouët, A. Abrutis, C. Jiménez, P. Odier, F. Weiss, IEEE Trans. Appl. Supercond. 19 (2009) 3184–3187.

[23] V. Cloet, J. Feys, R. Hühne, S. Hoste, I. Van Driessche, J. Solid State Chem. 182 (2009) 37–42.

[24] V. Cloet, P. Lommens, R. Hühne, K. De Buysser, S. Hoste, I. Van Driessche, J. Cryst. Growth (2011). doi:10.1016/j.jcrysgro.2011.04.029.

[25] Y.X. Zhou, X. Zhang, H. Fang, P.T. Putman, K. Salama, IEEE Trans. Appl. Supercond. 15 (2005) 2711–2714.

[26] M.S. Bhuiyan, M.P. Paranthaman, K. Salama, Superconductor. Sci. Technol. 19 (2006) R1–R21.

[27] I. Van Driessche, G. Penneman, E. Bruneel, S. Hoste, Pure Appl. Chem. 74 (2002) 2101–2109.

[28] I. Van Driessche, S. Cattoir, S. Hoste, Appl. Supercond. 2 (1994) 101–110.

[29] M.T. Le, W.J.M. Van Well, I. Van Driessche, S. Hoste, Appl. Catal. A: Gen. 267 (2004) 227–234.

[30] K. De Buysser, P. Lommens, C. De Meyer, E. Bruneel, S. Hoste, I. Van Driessche, Ceram.–Silikáty 48 (2004) 139–144.

[31] G.J. Vergote, C. Vervaet, I. Van Driessche, S. Hoste, S. De Smedt, J. Demeester, R.A. Jain, S. Ruddy, J.P. Remon, Int. J. Pharm. 219 (2001) 81–87.

[32] N. Van de Velde, D. Van de Vyver, O. Brunkahl, S. Hoste, E. Bruneel, I. Van Driessche, Eur. J. Inorg. Chem. 2 (2010) (2010) 233–241.

[33] B. Schoofs, V. Cloet, P. Vermeir, J. Schaubroeck, S. Hoste, I. Van Driessche, Superconductor Sci. Technol. 19 (2006) 1178–1184.

[34] P. Vermeir, I. Cardinael, M. Bäcker, J. Schaubroeck, E. Schacht, S. Hoste, I. Van Driessche, Superconductor Sci. Technol. 22 (2009) 075009.

[35] T. Thuy Tran, S. Hoste, G. Herman, N. Van de Velde, K. De Buysser, I. Van Driessche, J. Sol–Gel Sci. Technol. 51 (2009) 112–118.

[36] A.E. Martell, R.M. Smith, Critical Stability Constants, Vol. 2, Plenum press, New York, 1975.

[37] G. Yi, M. Sayer, J. Sol–Gel Sci. Technol. 6 (1996) 65–74.

[38] S.N.B. Hodgson, X. Shen, F.R. Sale, J. Mater. Sci. 35 (2000) 5275–5282.

[39] H. Kozuka, A. Higuchi, J. Mater. Res. 16 (2001) 3116–3123.

[40] J.J. Choi, J.H. Jang, D.S. Park, B.D. Hahn, W.H. Yoon, C. Park, Jpn. J. Appl. Phys. 46 (2007) 3549–3555.

[41] Z. Wang, J. Liu, T. Ren, L. Liu, Sensor Actuat. A Phys. 117 (2005) 293–300.

[42] G.T. Park, C.S. Park, J.J. Choi, J.W. Lee, H.E. Kim, J. Am. Ceram. Soc. 89 (2006) 2314–2316.

[43] W. Bouhamra, O. Bavbek, E. Alper, Chem. Eng. J. 73 (1999) 67–70.

[44] L. Molina, K. Knoth, S. Engel, B. Holzapfel, O. Eibl, Superconductor Sci. Technol. 19 (2006) 1200–1208.

[45] C. Jiménez, T. Caroff, L. Rapenne, S. Morlens, E. Santos, P. Odier, F. Weiss, J. Cryst. Growth 311 (2009) 3204–3210.

[46] I. Horcas, R. Fernández, J.M. Gómez-Rodríguez, J. Colchero, J. Gómez-Herrero, A.M. Baro, Rev. Sci. Instru. 78 (2007).

[47] R.W. Schwartz, T. Schneller, R. Waser, C.R. Chimie 7 (2004) 433–461.

[48] X.B. Zhu, S.M. Liu, H.R. Hao, P. Tong, C.X. Wang, W.H. Song, Y.P. Sun, K. Shi, Z.Y. Sun, S. Chen, Z. Han, Scr. Mater. 51 (2004) 659–663.

[49] X.B. Zhu, H.C. Lei, D.Q. Shi, L. Zhang, L. Wang, Y.P. Sun, W.H. Song, Z.R. Yang, J.H. Kim, R. Zeng, S.X. Dou, J. Yang, H.W. Gu, Phys. C Supercond. 467 (2007) 73–79.

[50] M.P. Paranthaman, M.S. Bhuiyan, S. Sathyamurthy, L. Heatherly, C. Cantoni, A. Goyal, Phys. C Supercond. 468 (2008) 1587–1590.